

Charge-carrier states and light absorption in ordered quantum dot superlattices

D. L. Nika,* E. P. Pokatilov,* Q. Shao, and A. A. Balandin†

Nano-Device Laboratory, Department of Electrical Engineering, University of California-Riverside, Riverside, California 92521, USA

(Received 20 May 2007; published 14 September 2007)

We have theoretically investigated the electron and hole energy spectra and light absorption in the three-dimensionally ordered quantum dots superlattices (QDS) made of the direct band-gap semiconductors. The calculations were performed for QDS of the rhombic symmetry with a substantial electron (hole) wave-function overlap using a one-band Hamiltonian for the electrons and six-band Hamiltonian for the holes. The obtained results were compared with the predictions of the simplified models for the uncoupled heavy, light, and split-off holes. It has been shown that the energy spectra of the electrons and holes in the ordered QDS are distinctively different from those in the single quantum dots (QD) or conventional quantum-well superlattices. The charge-carrier dispersion and localization are very sensitive to the quasicrystallographic directions defined by the dots, which play a role of the atoms in such QD supercrystal. We found that in the ordered QDS the oscillator strength for the interband optical transitions can be high for a relatively wide range of the photon energies. The obtained results are important for the proposed applications of QDS in solar cells, photodetectors, and thermoelectrics.

DOI: [10.1103/PhysRevB.76.125417](https://doi.org/10.1103/PhysRevB.76.125417)

PACS number(s): 73.21.-b, 73.22.-f, 73.21.La

I. INTRODUCTION

Nanostructures, such as multiple arrays of quantum dots (QD), have recently attracted significant attention owing to their unusual physical properties and proposed applications in photovoltaic solar cells,^{1,2} photodetectors,³⁻⁵ thermoelectric elements⁶⁻⁸ as well as electronic circuits based on the alternative state variables.^{9,10} Some of these applications can be implemented with the arrays of the uncoupled (or weakly coupled) and randomly distributed quantum dots—others require the long-range ordering of the quantum dots or precise control of the quantum dot position. While the properties of the single quantum dots made of different material systems have been extensively investigated theoretically,^{11,12} only a limited number of studies addressed the ensemble properties of the multiple arrays of quantum dots with a significant electron (or hole) wave-function overlap.^{13,14}

Three-dimensional (3D) ordering of the closely spaced QD in the quantum dot superlattices (QDS) results in the formation of the carrier minibands. The latter was demonstrated experimentally in a range of systems.^{15,16} Lazarenkova and Balandin¹³ reported a theoretical study where they calculated the electron states in the Kronig-Penny-type approach using a model confining potential, which led to the wave-function separation. Although their model is convenient for a simple calculation of the electronic states, it is hard to predict how closely the model potential replicates the realistic band offsets, particularly for the higher-energy minibands. In this paper we propose a rigorous approach for determining the electron and hole states in 3D ordered QDS and calculating the oscillator strength for the optical transitions in such structures. The proposed theoretical model and calculation procedure can be used for the prediction of the carrier transport and light absorption in the ordered QDS made of the direct band-gap semiconductors. There is a strong practical need in such a model taking into account the large scale of the experimental efforts focused on applications of QDS in photovoltaic cells, lasers, photodetectors, and thermoelectric elements.

The calculations, presented in this work, are carried out for InAs QD in a InGaAs host matrix. The selected material system is particularly interesting for a theoretical study because it was in the focus of many recent experimental investigations.¹⁷⁻²⁵ In the next section we present our theoretical formalism for determining the electron and hole energy dispersion in the ordered QDS. The hole states are treated using the six-band Hamiltonian, which allows us to take into account the interactions among the heavy, light, and spin-off hole bands. In Sec. III we report a comparison of our results with the prediction of the Lazarenkova and Balandin¹³ model for the electron states in QDS with the special wave-function separable potential. The calculation of the oscillator strength of the optical transitions in 3D ordered QDS are reported in Sec. IV. We give our conclusions in Sec. V.

II. ELECTRON AND HOLE STATES IN THE ORDERED QUANTUM DOT SUPERLATTICES

We consider a generic QDS with the dots ordered in all three dimensions. Although a fabrication of such 3D ordered QDS is still a major technological challenge, there have been a number of reports of achieving a nearly perfect 3D ordering in QDS.²⁶ It is expected that further progress in the self-assemble growth will result in a greater availability of the ordered QDS structures. Since we are mostly interested in the ensemble properties of QDS and the features, which originate from the dot-dot interaction (through the wave-function penetration), we assume the simplest orthorhombic symmetry for the dots with a corresponding rectangular prism unit cell (see the schematic in Fig. 1). The space symmetry group of such lattice is D_{2h}^{24} . In this structure, InAs QDs are located in the nodal points of the lattice filled with $\text{Ga}_{0.5}\text{In}_{0.5}\text{As}$, which acts as the barrier material. The dimensions of the QD sides are denoted by l_1, l_2, l_3 (where indices 1, 2, and 3 indicate axis $X, Y,$ and Z of the Cartesian coordinate system, respectively). The interdot distances (thick-

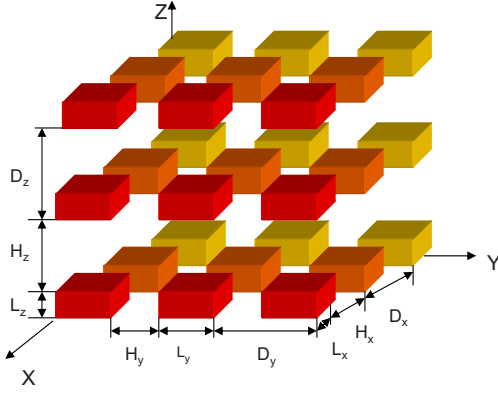


FIG. 1. (Color online) Schematic of the three-dimensionally ordered quantum dot superlattice showing notations for the quantum dot sizes and interdot spacing.

ness of the barriers) are denoted by h_1 , h_2 , and h_3 . The translation periods of the lattice are $d_i = l_i + h_i$ ($i=1, 2, 3$) with the lattice basis vectors $\vec{a}_1(a_1, 0, 0)$, $\vec{a}_2(0, a_2, 0)$, and $\vec{a}_3(0, 0, a_3)$, where $a_i = d_i$ ($i=1, 2, 3$).

The basis vectors of the reciprocal lattice, required for the construction of the quasi Brillouin zone (QBZ), are $\vec{b}_1(b_1, 0, 0)$, $\vec{b}_2(0, b_2, 0)$, and $\vec{b}_3(0, 0, b_3)$, where $b_i = 2\pi/d_i$ ($i=1, 2, 3$). QBZ in QDS supracrystal, i.e., 3D ordered QDS, is analogous to the conventional Brillouin zone for crystal solids, which is defined as a Wigner-Seitz cell of the reciprocal lattice. In the QDS supracrystal, the quantum dots play a role of the atoms. In the atomic crystal lattices the exact wave functions of the charge carriers cannot be obtained due to the difficulties of finding the actual periodical lattice potentials. In QDS the periodic potential is well defined and the solutions of the Schrödinger equation can be presented explicitly. In our analysis we consider the electron and hole states separately due to a sufficiently large energy gap between the electron and hole states in QD, which is increased by the size quantization and reaches a value ~ 0.64 eV for the considered dimensions. Owing to the translational symmetry in the ordered QDS, the electron (hole) envelope wave functions, defined as in the effective mass approximation, obeys the relation

$$\Psi_n^{e,h}(\vec{r} + \vec{a}) = \Psi_n^{e,h}(\vec{r}) e^{i\vec{k}\vec{a}}. \quad (1)$$

Here \vec{k} is the quasicontinuous wave vector of the electron (hole), n is the quantum number of the size-quantized electron (hole) states, $\vec{a} = N_1\vec{a}_1 + N_2\vec{a}_2 + N_3\vec{a}_3$ is the lattice vector, where N_1 , N_2 , and N_3 are the arbitrary integer numbers. The maximum value of \vec{k} is restricted by the QBZ boundaries.

The one-band Schrödinger equation for an electron in QDS can be written as

$$\left(-\frac{\hbar^2}{2} \nabla \frac{1}{m^e(\vec{r})} \nabla + V^e(\vec{r}) \right) \Psi_n^e(\vec{r}) = E_n^e \Psi_n^e(\vec{r}), \quad (2)$$

where $V^e(\vec{r})$ is the potential energy, $m^e(\vec{r})$ is the electron effective mass, and \hbar is the Planck constant. The potential energy $V^e(\vec{r})=0$ and the electron mass $m^e(\vec{r})=m^e(\text{InAs})$

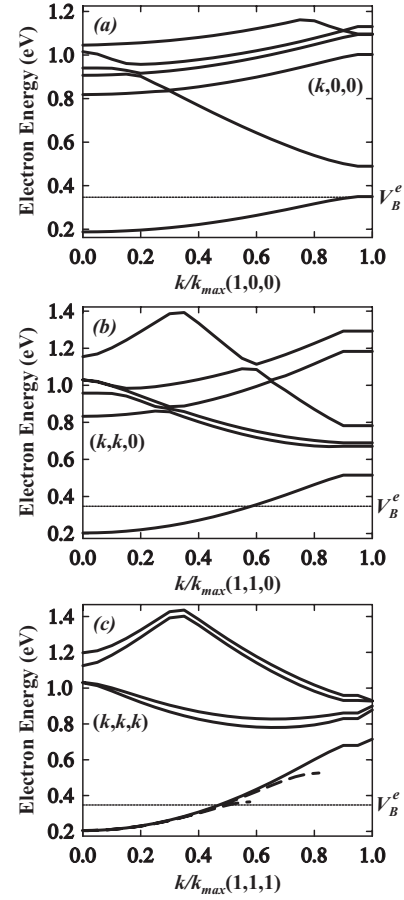


FIG. 2. Electron dispersion in InAs/Ga_{0.5}In_{0.5}As QDS (a) along the (1,0,0) quasicrystallographic direction with the QDS dimensions $l_x=5.0$ nm, $l_y=5.5$ nm, $l_z=6.0$ nm, and $h_x=h_y=h_z=2.0$ nm; (b) along (1,1,0) with the dimensions $l_x=l_y=5.0$ nm, $l_z=6.0$ nm, and $h_x=h_y=h_z=2.0$ nm; (c) along (1,1,1) with the dimensions $l_x=l_y=l_z=5.0$ nm and $h_x=h_y=h_z=2.0$ nm. The electron energies are measured from the conduction band bottom. The values of the potential barrier are shown in all figures by the straight line.

$=0.026m_0$ inside the QD boundaries defined as $|x_i - (\vec{a})_i| \leq \frac{l_i}{2}$ (the coordinate origin is chosen in the center of QD). Outside of the QD boundaries (inside the barrier layers) defined as $\frac{l_i}{2} \leq |x_i - (\vec{a})_i|$, the following values of the potential and mass are assumed: $V^e(\vec{r}) = V_B^e = \text{const}$ and $m^e(\vec{r}) = m^e(\text{Ga}_{0.5}\text{In}_{0.5}\text{As}) = 0.0435 m_0$, where m_0 is the electron mass in vacuum. Eq. (2) with the periodic boundary conditions given by Eq. (1) was solved numerically using the finite difference method.

The electron energy dispersions, calculated for three different QDS along three quasicrystallographic directions, are presented in Fig. 2. The results are shown for $l_x=5$ nm, $l_y=5.5$ nm, $l_z=6$ nm, and $\vec{k}=(k, 0, 0)$ [panel (a)]; $l_x=5$ nm, $l_y=5$ nm, $l_z=6$ nm, and $\vec{k}=(k, k, 0)$ [panel (b)]; and $l_x=5$ nm, $l_y=5$ nm, $l_z=5$ nm, and $\vec{k}=(k, k, k)$ [panel (c)]. The barrier thicknesses are $h_x=h_y=h_z=2$ nm for all of the considered QDS. The maximum values of the electron wave vector k used for normalization in Fig. 2 are $k_{\text{max}}(1, 0, 0) = 0.448 \text{ nm}^{-1}$, $k_{\text{max}}(1, 1, 0) = 0.663 \text{ nm}^{-1}$, and $k_{\text{max}}(1, 1, 1)$

$=0.776 \text{ nm}^{-1}$. The electron energies are counted from the bottom of the potential well.

One can see from Fig. 2 that the common features for all considered QDS include the strong size quantization of the electron energy spectra and appearance of the relatively wide minibands for all n . The width of the lowest miniband is on the order of $6.5k_B T$ at room temperature, where k_B is the Boltzman constant and T is an absolute temperature. This is a large value, which implies that the electrons move rather freely though the miniband. Another observation is that only the lowest (ground-state) miniband energies are below the potential barrier level, i.e., $\varepsilon(k) < V_B^e$ (with the exception of the very large electron wave vectors k). The value of the potential barrier for the chosen system is $V_B^e = 0.83[E_g(\text{Ga}_{0.5}\text{In}_{0.5}\text{As}) - E_g(\text{GaAs})] = 0.347 \text{ eV}$.²⁷ The energies of all excited minibands are larger than the potential barrier height V_B^e . The electron energy dispersion for the excited minibands differs strongly from the free-electron energy dispersion or the near-parabolic dispersion in the conduction band of bulk GaAs crystal. All dispersion branches are double degenerate except for the first excited level shown in Fig. 2(c), which is fourfold degenerate. The energy dispersion in the ground state miniband is near parabolic for a wide interval of k in the considered directions, i.e., (1,0,0), (1,1,0), and (1,1,1). For comparison, in Fig. 2(c) we also show with the dashed lines the energy dispersion for the ground mini-

band in ordered QDS with the cubic QD ($l_x=l_y=l_z=5 \text{ nm}$) along (1,0,0) and (1,1,0) quasicrystallographic directions. It is clear from this figure that the equal-energy surfaces in k space are nearly isotropic. Note that the lowest levels play a major role in the kinetic processes at low and medium temperatures and moderate electron concentrations (characterized by the Fermi energy smaller than 0.5 eV). The non-monotonic behavior of the dispersion curves for all exited minibands leads to a strong dependence of the electron velocity on the value of the electron wave vector k as well as appearance of the electron states with the negative velocities, which correspond to the region of the dispersion curves with negative slopes.

The hole energies E_n^h and wave functions $\Psi_n^h(\vec{r})$ were obtained from the numerical solution of the Schrödinger equation with the six-band Hamiltonian, which takes into account the interactions among the heavy, light, and spin-off hole bands. The Hamiltonian is written as^{28,29}

$$\hat{H}_n^h \vec{\Psi}_n^h = E_n^h \vec{\Psi}_n^h, \quad (3)$$

where

$$\hat{H}_h = \begin{vmatrix} \hat{H}_{XYZ}(\vec{r}_h) & 0 \\ 0 & \hat{H}_{XYZ}(\vec{r}_h) \end{vmatrix} + \hat{H}_{\text{SO}}(\vec{r}_h), \quad (4)$$

$$\hat{H}_{XYZ}(\vec{r}_h) = \frac{\hbar^2}{2m_0} \begin{vmatrix} \varepsilon'_v - \hat{k}_x \beta_l \hat{k}_x - \hat{k}_x^\perp \beta_h \hat{k}_x^\perp & -3(\hat{k}_x \gamma_3^+ \hat{k}_y + \hat{k}_y \gamma_3^- \hat{k}_x) & -3(\hat{k}_x \gamma_3^+ \hat{k}_z + \hat{k}_z \gamma_3^- \hat{k}_x) \\ -3(\hat{k}_x \gamma_3^- \hat{k}_y + \hat{k}_y \gamma_3^+ \hat{k}_x) & \varepsilon'_v - \hat{k}_y \beta_l \hat{k}_y - \hat{k}_y^\perp \beta_h \hat{k}_y^\perp & -3(\hat{k}_y \gamma_3^+ \hat{k}_z + \hat{k}_z \gamma_3^- \hat{k}_y) \\ -3(\hat{k}_x \gamma_3^- \hat{k}_z + \hat{k}_z \gamma_3^+ \hat{k}_x) & -3(\hat{k}_y \gamma_3^- \hat{k}_z + \hat{k}_z \gamma_3^+ \hat{k}_y) & \varepsilon'_v - \hat{k}_z \beta_l \hat{k}_z - \hat{k}_z^\perp \beta_h \hat{k}_z^\perp \end{vmatrix}, \quad (5)$$

$$\hat{H}_{\text{SO}}(\vec{r}_h) = \frac{\Delta(\vec{r}_h)}{3} \begin{vmatrix} 0 & -i & 0 & 0 & 0 & 1 \\ i & 0 & 0 & 0 & 0 & -i \\ 0 & 0 & 0 & -1 & i & 0 \\ 0 & 0 & -1 & 0 & i & 0 \\ 0 & 0 & -i & -i & 0 & 0 \\ 1 & i & 0 & 0 & 0 & 0 \end{vmatrix}. \quad (6)$$

In Eqs. (4)–(6), we define $\varepsilon'_v = \varepsilon_v - \delta/3$, $\hat{k} = -i\vec{\nabla}$, $\hat{k}_{x,y,z}^\perp = \hat{k} - \hat{k}_{x,y,z}$; $\Delta(\vec{r}_h) = \hbar^2 \delta(\vec{r}_h)/(2m_0)$ is the spin-orbit splittings of the valence band, $E_v(\vec{r}_h) = \hbar^2 \varepsilon_v(\vec{r}_h)/(2m_0)$ is the energy of the valence band maximum, and

$$\beta_l = \beta_l(\vec{r}_h) = \gamma_1(\vec{r}_h) + 4\gamma_2(\vec{r}_h),$$

$$\beta_h = \beta_h(\vec{r}_h) = \gamma_1(\vec{r}_h) - 2\gamma_2(\vec{r}_h),$$

$$\gamma_3^\pm = \gamma_3^\pm(\vec{r}_h) = \gamma_3(\vec{r}_h) \pm \chi(\vec{r}_h),$$

$$\chi(\vec{r}_h) = [2\gamma_2(\vec{r}_h) + 3\gamma_3(\vec{r}_h) - \gamma_1(\vec{r}_h)]/3. \quad (7)$$

Inside the QD, the Luttinger parameters $\gamma_i(\vec{r}_h) = \gamma_i(\text{InAs})$ ($i=1,2,3$), $\Delta(\vec{r}_h) = \Delta(\text{InAs})$, and $E_v(\vec{r}_h) = E_v(\text{InAs})$, while outside the QD (inside the barrier materials) $\gamma_i(\vec{r}_h) = \gamma_i(\text{Ga}_{0.5}\text{In}_{0.5}\text{As})$, $\Delta(\vec{r}_h) = \Delta(\text{Ga}_{0.5}\text{In}_{0.5}\text{As})$, and $E_v(\vec{r}_h) = E_v(\text{Ga}_{0.5}\text{In}_{0.5}\text{As})$. The material parameters required for the calculation of the hole energy spectra were taken from Ref. 30.

The energy dispersion for the holes in the ordered QDS (with the same dimensions as those in Figs. 2) along the quasicrystallographic directions (1,0,0), (1,1,0), and (1,1,1) are shown in Figs. 3(a)–3(c), respectively. The energy is counted from the bottom of the valence band. Comparing Figs. 2 and 3, one can see that the quantization of the hole-energy spectra is weaker than that of the electron spectra. The ground state minibands in all considered cases have energies smaller than 0.05 eV. The spin-orbit interaction splits the multifold degenerate hole-energy levels into the branches with the similar energies in the narrow region of a few meV.

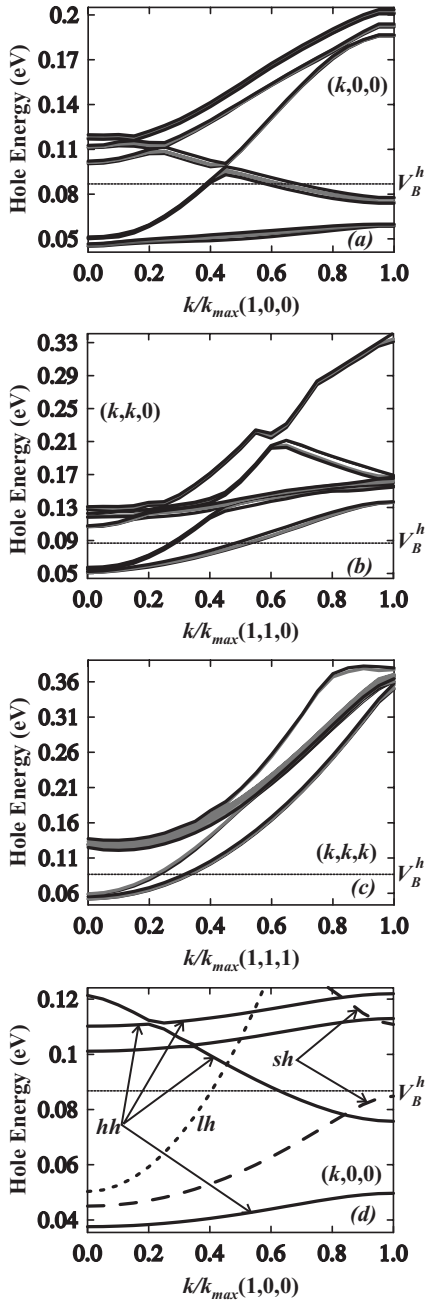


FIG. 3. Hole dispersion obtained within the six-band model in InAs/Ga_{0.5}In_{0.5}As QDS (a) along the (1,0,0) quasicrystallographic direction with the QDS dimensions $l_x=5.0$ nm, $l_y=5.5$ nm, $l_z=6.0$ nm, and $h_x=h_y=h_z=2.0$ nm; (b) along (1,1,0) with the dimensions $l_x=l_y=5.0$ nm, $l_z=6.0$ nm, and $h_x=h_y=h_z=2.0$ nm; (c) along (1,1,1) with the dimensions $l_x=l_y=l_z=5.0$ nm and $h_x=h_y=h_z=2.0$ nm. (d) The dispersion of heavy (solid lines), light (dotted lines), and spin-off (dashed lines) holes along (1,0,0) with the same dimensions as in (a). The hole energies are measured from the top of the valence band and shown with the positive sign.

Along the (1,0,0) quasicrystallographic direction the hole energies of the lowest branch are smaller than the valence band barrier energy $E_B^h=0.086$ eV for all values of the hole wave vector k . Thus, the hole wave function of the split ground-state miniband is mostly located in the potential well. Along the (1,1,0) and (1,1,1) directions the hole energy rapidly in-

creases with increasing k and the holes become weakly localized or nearly free states. Along the (1,0,0) and (1,1,0) directions the dispersion curves have the minimum and maximum values whereas along the (1,1,1) direction the hole energy increases monotonically with increasing of k (as in bulk crystals). The revealed differences among the dispersion curves along various directions are expected to manifest themselves in the spatial anisotropy of the kinetic coefficients in QDS.

Figure 3(d) demonstrates the strength of the hole state intermixing by depicting the difference between the hole energy spectra obtained using the six-band Hamiltonian, which takes into account the interactions between the hole bands, and the one-band Hamiltonians for the independent heavy, light, and spin-off holes. The heavy holes (indicated by solid lines) manifest small size-quantization (around 10 meV for the excited states) and weak dispersion while the light and spin-off holes show large size quantization and strong dispersion. All energy levels of these holes are twofold degenerate. Only the energies of the ground states of the heavy and those of the interacting “six-band” holes are similar. The independent systems of the weakly dispersive heavy holes and strongly dispersive light and spin-off holes transform, in the case of interacting “six-band” holes, into a system of the four weakly dispersive lowest levels and strongly dispersive higher levels with $n > 4$. Thus, the properties of the light, spin-off, and heavy holes manifest themselves in each dispersion curve of the interacting “six-band” holes for $n > 4$.

III. COMPARISON WITH THE SEMIANALYTICAL MODEL FOR THE QUANTUM DOT SUPERLATTICE

It is illustrative to compare the electronic dispersion obtained for the ordered QDS calculated using the approach outlined in Sec. II with the prediction of the semianalytical model,¹³ based on the approximate confining potential, which allows for the electron wave-function separation along the three coordinates. The model has been applied for the calculation of the minibands in QDS-based solar cells.³¹ In order to perform the comparison, one must assume that the confining potential is written as a sum of three independent periodic functions of coordinates x , y , and z (with periods of d_x , d_y , and d_z), i.e., $V(\mathbf{r})=V_x(x)+V_y(y)+V_z(z)$, where each component is given as

$$V_\xi(\xi) = \begin{cases} 0 & \text{if } |\xi - \eta_\xi d_\xi| \leq L_\xi d/2, \\ V_0 & \text{if } |\xi - \eta_\xi d_\xi| > L_\xi d/2. \end{cases} \quad (8)$$

Here η_ξ are the integer numbers and subscript ξ denotes a particular coordinate axis. This choice of potential results in nonuniform barrier height (larger potentials in the corner) but allows one to separate the carrier motion along three coordinate axes. As shown in Ref. 13, the solution of the Schrödinger equation for the QDS with the potential of Eq. (8) has the Kronig-Penney-type form and can be written as

$$\begin{aligned} \cos(q_\xi d_\xi) = & \cos(k_\xi^W L_\xi) \cos(k_\xi^B H_\xi) - \frac{1}{2} \left(\frac{k_\xi^B m_W^*}{k_\xi^W m_B^*} + \frac{k_\xi^W m_B^*}{k_\xi^B m_W^*} \right) \\ & \times \sin(k_\xi^W L_\xi) \sin(k_\xi^B H_\xi) \quad \text{if } E_\xi \geq V_0, \end{aligned} \quad (9a)$$

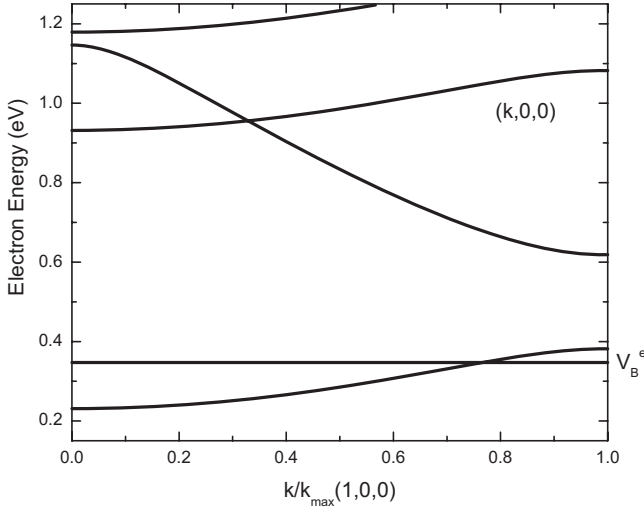


FIG. 4. Electron dispersion obtained within the semianalytical model which assumes that the confining potential can be presented as $V(\mathbf{r})=V_x(x)+V_y(y)+V_z(z)$. The results are shown for QDS with the same dimensions as in Fig. 3(a).

$$\cos(q_\xi d_\xi) = \cos(k_\xi^W L_\xi) \cosh(k_\xi^B H_\xi) - \frac{1}{2} \left(-\frac{k_\xi^B m_W^*}{k_\xi^W m_B^*} + \frac{k_\xi^W m_B^*}{k_\xi^B m_W^*} \right) \times \sin(k_\xi^W L_\xi) \sinh(k_\xi^B H_\xi) \quad \text{if } 0 < E_\xi < V_0, \quad (9b)$$

where

$$k_\xi^B = \frac{\sqrt{2m_B^*|E_\xi - V_0|}}{\hbar}, \quad k_\xi^W = \frac{\sqrt{2m_W^*|E_\xi|}}{\hbar}. \quad (10)$$

Here m_B^* and m_W^* are the effective masses inside the barrier and quantum dot, correspondingly. One can calculate the electron dispersion in the ordered QDS with this simplifying potential as $E(\mathbf{q})=E_x(q_x)+E_y(q_y)+E_z(q_z)$.

Figure 4 shows the electron dispersion relation obtained with the model potential of Eq. (8). The results are obtained for the ordered QDS with the same structure and material parameters as those depicted in Fig. 2(a). A direct comparison of the dispersion relations in Fig. 4 and Fig. 2(a) indicates that the results agree well for the small energies (lowest minibands) but start to deviate for the above-the-barrier states. The width of the lowest miniband is $5.8k_B T$ at room temperature. This value is in good agreement with our calculations with an actual equal-height potential. Thus, it is safe to use the model potential and the Kronig-Penny-type solution for the below-the-barrier states in the conduction band of the ordered QDS.

IV. ANALYSIS OF THE ELECTRONIC STATES IN THE ORDERED QUANTUM DOT SUPERLATTICES

In order to understand the nature of the electron and hole states in the ordered QDS and their differences from those in conventional quantum-well superlattices and bulk crystals, we calculated the electron (hole) density distributions in the ordered QDS. The knowledge of the charge-carrier density distributions can help to elucidate the specifics of the charge-

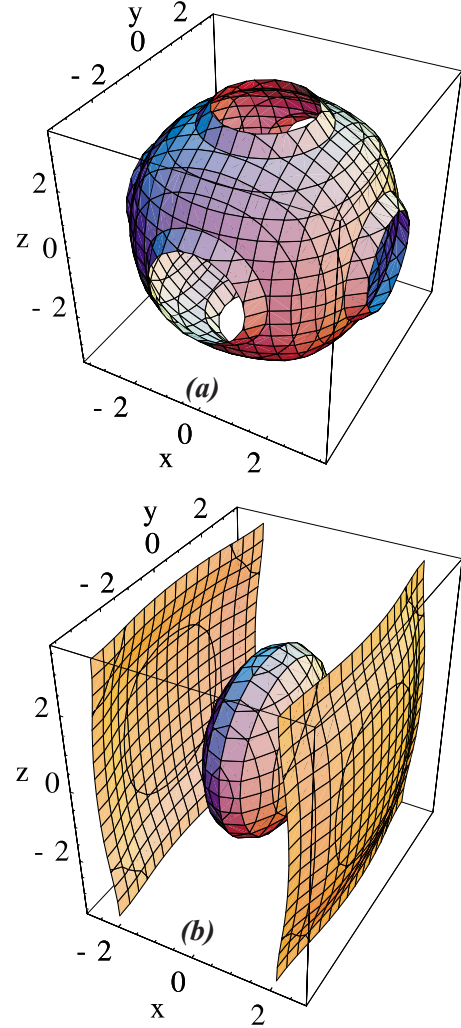


FIG. 5. (Color online) Constant surface of the electron density function $|\Psi_{n=1}^e|^2 = \frac{c}{d_1 d_2 d_3}$ in the ordered QDS with the dimensions $l_x=l_y=l_z=5$ nm and $h_x=h_y=h_z=2$ nm for (a) $c=1.0$ and the electron wave vector $k=0.0$; and (b) $c=0.5$ (outside) and $c=2.0$ (toroidal surface) for $k=k_{\max}(1,0,0)$.

carrier transport and light absorption by such artificial supercrystals. The electron density functions in the ordered QDS with the QD dimensions $l_x=l_y=l_z=5$ nm and the barrier thicknesses $h_x=h_y=h_z=2$ nm are shown in Figs. 5(a), 5(b), 6(a), and 6(b) for $k=0$ and $k=k_{\max}$ for the quasicrystallographic directions (1,0,0), (1,1,0), and (1,1,1).

Figure 5(a) shows the constant surface of the electron function $|\Psi_{n=1}^e|^2 = \frac{c}{V_0}$, where $V_0=d_1 d_2 d_3$ is the volume of the unit cell of the ordered QDS and $c=1.0$. The cube plotted in Fig. 5(a) represents the unit cell with the sides $d_1=d_2=d_3=7$ nm. The potential quantum well with the sides $l_x=l_y=l_z=5$ lies inside the cube. The surface $|\Psi_{n=1}^e(\vec{r}, k=0)|^2 = \text{const}$ is the invariant function of the QDS symmetry group. The regions of the high density of the electron wave function are represented by the spherical surfaces, while the regions of the lower density are represented by the channel-like surfaces joined with the cube faces. The latter indicates that the electron wave functions penetrate through the barriers in the

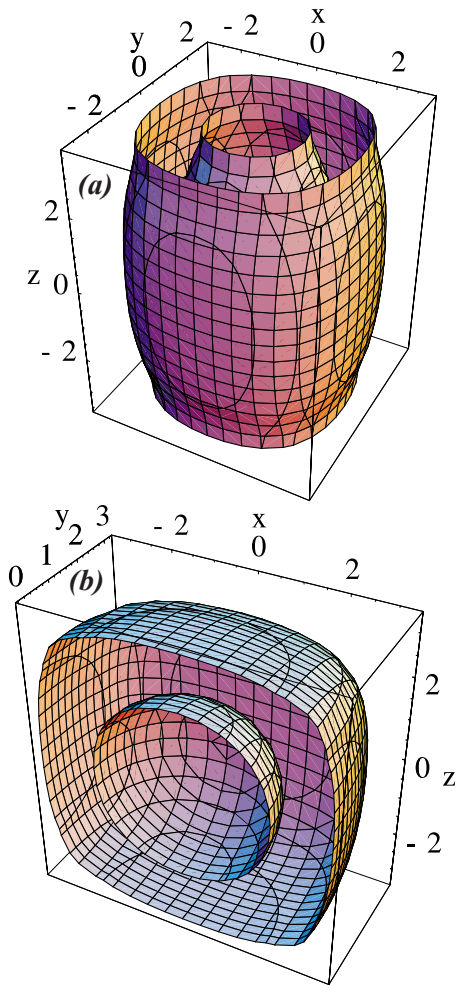


FIG. 6. (Color online) Constant surface of the electron density function for (a) $c=0.7$ (outside surface) and $c=2.2$ (inside surface) for the electron wave vector $k=k_{\max}(1,0,0)$; and for (b) $c=0.2$ (outside surface) and $c=3.0$ (inside surface) for $k=k_{\max}(1,1,1)$. The QDS dimensions are the same as in Fig. 5.

middle of the dot and periodically repeat themselves in all unit cells. The electron density function for $k=k_{\max}(1,0,0)$ is presented in Fig. 5(b) for $c=0.5$ and $c=2.0$. A comparison of Figs. 5(a) and 5(b) indicate that the electron density distribution in QDS strongly depends on the value of the electron wave vector k . The high-density core of the electron function $|\Psi_{n=1}^e|^2$ is spherical for $k=0$ while it is ellipsoidal for $k=k_{\max}(1,0,0)$. The channel-like surfaces along three directions (at $k=0$) transform into the channel-like surfaces along two directions (0,1,0) and (0,0,1). The shape of the equal-density surfaces reflect the symmetry reduction introduced by the nonzero wave vector k . At $k=k_{\max}(1,0,0)$ the electron density is equal to zero in the middle of the barrier on the (Y,Z) plane and the electron energy reaches maximum value while the electron velocity becomes zero, i.e., $v(k) = (\partial \varepsilon(k)) / (\hbar \partial k)|_{k_{\max}} = 0$.

The dependence of the electron density function on k along the (1,1,0) quasicrystallographic direction is somewhat analogous. In this case, the electron density is compressed in two directions (1,0,0) and (0,1,0) while the linkage channel-

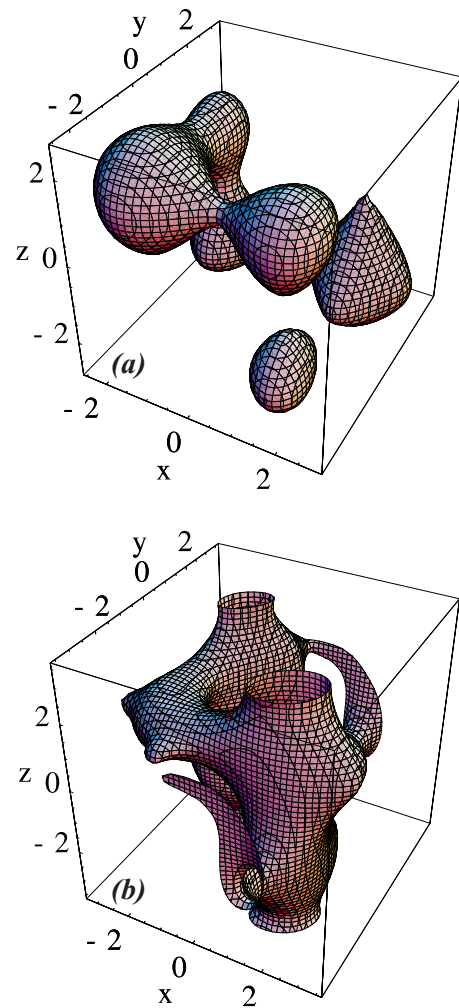


FIG. 7. (Color online) Constant surface of the hole density function $|\Psi_{n=12}^h|^2 = \frac{c}{d_1 d_2 d_3}$ in the ordered QDS with the dimensions $l_x = l_y = l_z = 5$ nm and $h_x = h_y = h_z = 2$ nm for (a) $c=2.0$ and the hole wave vector $k=0$; and (b) $c=1.7$ for $k=k_{\max}(1,1,1)/2$.

like region remains in the (0,0,1) quasicrystallographic direction as shown in Fig. 6(a) for $c=0.7$ and $c=2.2$. If k_{\max} is chosen along the (1,1,1) direction the electron density function is compressed in all three directions [depicted in Fig. 6(b) for $c=0.2$ and $c=3.0$]. It is interesting to note that for the same value of the electron wave vector k , the electron localization is stronger when k is along the (1,1,1) direction. Although not shown in the figures, the electron density functions of the excited states have more complicated shapes than those of the ground states. The equal density surfaces for the excited states do not form closed contours inside the unit cell cubes, which indicate that the electrons are completely delocalized and occupy the whole QDS.

The constant surfaces of the hole density functions $|\Psi_n^h|^2 = \frac{c}{V_0}$ for different excited states are shown in Figs. 7(a) and 7(b). Figure 7(a) shows the surface with $c=2.0$ for $n_h=12$ and $k=0$ for the quasicrystallographic direction (1,1,1). The equal density surfaces in this case are connected in many points. The holes with the densities indicated in the plots (or higher densities) are localized inside of the unit cell of QDS.

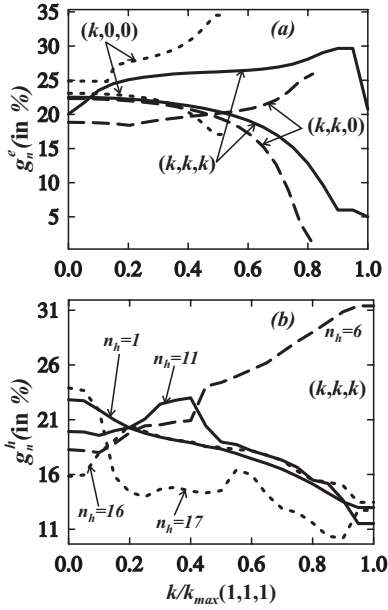


FIG. 8. Normalized “delocalization” function $g_n^{e,h}(k) = \int_{\Omega_B} |\Psi_n^{e,h}(\vec{r})| d\vec{r}$ as a function of the electron wave vector k for (a) the two lowest electron minibands ($n=1, 2$); and (b) several hole minibands ($m=1, 6, 11, 16, 17$) in InAs/Ga_{0.5}In_{0.5}As QDS with the dimensions $l_x=l_y=l_z=5$ nm and $h_x=h_y=h_z=2$ nm.

Figure 7(b) presents the hole density function surface, which corresponds to the density $|\Psi_n^h|^2 \geq \frac{1.7}{V_0}$ at $k=k_{\max}(1,1,1)/2$. One can see from this figure that the “open channels” for the hole transport through the ordered QDS do exist.

In order to quantitatively characterize the wave-function penetration in the neighboring unit cells of the ordered QDS cells we calculated the dependence of the “delocalization” functions $g_n^{e,h}(k) = \int_{\Omega_B} |\Psi_n^{e,h}(\vec{r})| d\vec{r}$ on the wave vector k for the electrons [Fig. 8(a)] and holes [Fig. 8(b)]. The values of the normalized functions $g_n^{e,h}(k)$ are given in percent. The integration in $g_n^{e,h}(k)$ is performed over the whole barrier volume Ω_B between the QD. It follows from Fig. 8(a) that the function g^e for the ground electron miniband reaches its maximum value at $k=0$, and decreases with increasing k for all directions of the electron motion. The electron wave function for $k=k_{\max}(1,1,1)$ practically does not penetrate the barrier material and the electron is localized inside the QD. A different situation is observed for the excited miniband $n=3$. For both quasicrystallographic directions (1,0,0) and (1,1,0) the confinement weakens with increasing wave vector k . For the (1,1,1) direction only the confinement enhances slightly for the wave vector k close to k_{\max} . The “delocalization” functions $g_n^h(k=0)$ for the hole states are smaller than those for the electrons states, and generally decrease with increasing k . The stronger hole localization is explained by the larger effective masses of the holes as compared to those of the electrons. The described properties of the electron and hole wave functions in QDS strongly influence the matrix elements of the electron (hole) interaction with photons and phonons.

V. OSCILLATOR STRENGTH OF THE OPTICAL TRANSITIONS IN THE QUANTUM DOT SUPERLATTICES

The efficiency of the light absorption ability of a nanostructure can be illustrated, to some degree, by the oscillator strength of the optical transitions. For the calculation of the oscillator strength of the band-to-band (hole-electron) transitions we assumed that the electron momentum is equal to the hole momentum in absolute value and have the opposite direction, i.e., $\vec{k}_e = -\vec{k}_h$. The latter is a valid assumption due to the small value of the photon momentum. The oscillator strength of the transition induced by the light polarized along the X axis, which leads to the generation of the electron-hole pair, is given by

$$f(n_e, n_h) = \frac{E_p}{E_{e-h}^{n_e, n_h}} = \sum_{\alpha} \left(\left| \int_V [\Psi_{\text{Re},e}^{n_e, \alpha}(\vec{r}) \Psi_{\text{Im},e}^{n_e, \alpha}(\vec{r}) - \Psi_{\text{Im},e}^{n_e, \alpha}(\vec{r}) \Psi_{\text{Re},e}^{n_e, \alpha}(\vec{r})] d\vec{r} \right|^2 + \left| \int_V [\Psi_{\text{Re},e}^{n_e, \alpha}(\vec{r}) \Psi_{\text{Im},h}^{n_h, \alpha}(\vec{r}) + \Psi_{\text{Im},e}^{n_e, \alpha}(\vec{r}) \Psi_{\text{Re},h}^{n_h, \alpha}(\vec{r})] d\vec{r} \right|^2 \right), \quad (11)$$

where E_p is the Kane energy, $E_{e-h}^{n_e, n_h}$ is the energy of the electron-hole pair with the quantum numbers n_e, n_h , $\Psi_{\text{Re},e}^{n_e, \alpha}(\vec{r})$ and $\Psi_{\text{Im},e}^{n_e, \alpha}(\vec{r})$ are the real and imaginary parts of the electron wave function in the state with the quantum number n_e , $\Psi_{\text{Re},1,h}^{n_h, \alpha}(\vec{r})$ and $\Psi_{\text{Im},1,h}^{n_h, \alpha}(\vec{r})$ are the real and imaginary parts of the hole wave-function component $\Psi_{1,h}^{n_h, \alpha}(\vec{r})$ in the state with the quantum number n_h, α is the index of degeneracy. We derived Eq. (11) using the formalism described in Ref. 32.

The dependence of the oscillator strengths on the photon energy is shown in Figs. 9(a)–9(c) for the different parameters of the quantum dots and various QDS quasicrystallographic orientations: (1,0,0), (1,1,0), and (1,1,1). Figure 9 shows the oscillator strength in QDS with the dimensions $l_x=5$ nm, $l_y=5.5$ nm, $l_z=6$ nm, and $h_x=h_y=h_z=2$ nm for (1,0,0) orientation of QDS. The solid lines in this plot correspond to the transitions involving the twofold degenerate ground electron state and 20 hole levels. The energy of the higher electron states are considerably larger than the electron ground-state energy and, therefore, do not affect the oscillator strength. The higher hole levels ($n > 20$) do not influence the oscillator strength owing to the strong oscillatory nature of their wave functions. Figures 9(b) and 9(c) present the oscillator strength for two other orientations of QDS. The electron-momentum independent oscillator strength can be obtained by averaging of the dependencies presented in Figs. 9(a)–9(c) over all directions. Since the general trends for the oscillator strength are similar for all three quasicrystallographic directions, the averaged oscillator strength is expected to be very close to those depicted in Figs. 9(a)–9(c).

The dashed lines in Figs. 9(a)–9(c) correspond to the oscillator strength for the transitions between the ground-state

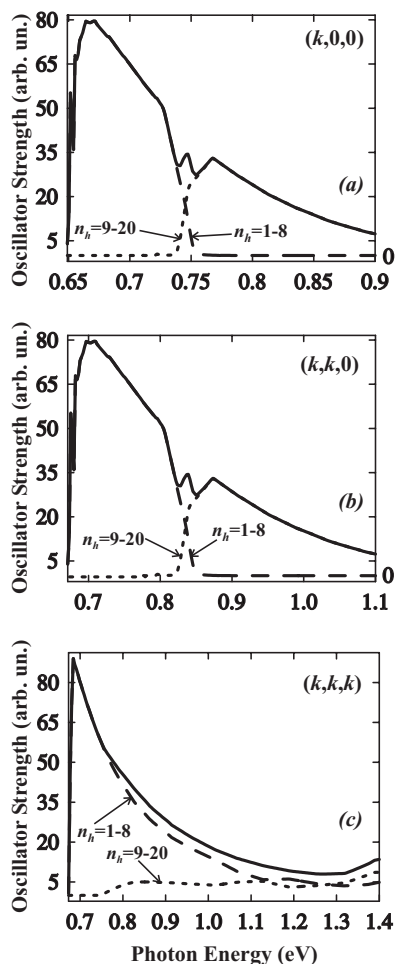


FIG. 9. Oscillator strength of the electron-hole optical transitions as a function of the photon energy in InAs/Ga_{0.5}In_{0.5}As QDS with the dimensions (a) $l_x=5$ nm, $l_y=5.5$ nm, $l_z=6$ nm, and $h_x=h_y=h_z=2$ nm for the (1,0,0) orientation; (b) $l_x=5$ nm, $l_y=5$ nm, $l_z=6$ nm, and $h_x=h_y=h_z=2$ nm for (1,1,0); and (c) $l_x=l_y=l_z=5$ nm, $l_z=6$ nm, and $h_x=h_y=h_z=2$ nm for (1,1,1).

electrons and the eight lowest hole levels while the dotted lines correspond to the transitions between the ground-state electrons and the 12 hole levels with the quantum numbers $n_h=9-20$. It is interesting to see from these plots that the higher hole levels begin to participate in the transitions as the energy exceeds ~ 0.74 eV while the oscillator strength for the transitions involving eight lower levels decrease to zero for the energy $\hbar\omega > 0.75$ eV. Both the dashed and dotted curves manifest a maximum value, i.e., the dashed curves attain it at the photon energy of $\hbar\omega=0.65$ eV while the dotted curves reach it at about $\hbar\omega=0.75$ eV. The resulting oscillator strength dependence on photon energy manifests a general monotonic decrease but remains rather high in a relatively wide interval pertinent to the infrared and visible light absorption. The latter suggest that such nanostructures can be

particularly efficient for the infrared photodetector applications.

Another important application of QDS, which can greatly benefit from the formation of the minibands and increased oscillator strength is QD-based lasers. The Auger recombination is the main reason for the decrease of the inverse charge population in QD. The population inversion is a required condition for generating the laser radiation.³³ The higher density of QD and formation of the minibands reinforce the effect of the stimulated emission and reduces the radiation relaxation time of the electron-hole pairs. This allows one to obtain strong laser radiation at the lower pump levels.³⁴ The miniband formation leads to the higher carrier mobility, lower critical current density for electrical injection and improved monochromaticity of the radiated light.

VI. CONCLUSIONS

We calculated the energy dispersion for the electrons and holes in the ordered quantum dot superlattices for the case of InAs/Ga_{0.5}In_{0.5}As material system. From the obtained dispersion we determined the oscillator strength of the optical transitions in such nanostructures. It has been shown that the energy dispersion for the ground electron and hole states in the quantum dot superlattices are nearly parabolic. The energy of the electron excited states at zone center $k=0$ (size-quantized levels) is significantly larger than the potential barrier for the electrons and practically do not play any role in the optical and kinetic processes. The energy spectra of the hole states obtained within the framework of the six-band Hamiltonian possess the features of the hybrid “heavy,” “light,” and “split-off” hole bands. The lowest energy levels manifest the weak energy dispersions similar to the “heavy holes” while the excited states display the strong dispersions as the “light” and “split-off” holes. It has been established that in the considered ordered QDS, with the selected geometrical parameters, heights of the potential barriers and values of effective masses, both electrons and holes penetrate through the entire barrier layer thicknesses. Specifically, it has been found via averaging of the charge densities that in the barriers there are approximately 25% of the total electron and 18% of the total hole charge. The relevance of the developed model for optimization of QDS for applications in solar cells, photodetectors, and lasers was also discussed.

ACKNOWLEDGMENTS

The work at UCR was supported, in part, through the AFOSR subcontract on the Optimized Quantum Dot Superlattice Structures for High Efficiency Photovoltaic Cells and Photodetectors. One of the authors (A.A.B.) is thankful to A. Fedoseyev and M. Turowski, CFD Research Corporation for useful discussions. The authors also acknowledge the support of the U.S. Civil Research and Development Foundation (CRDF).

*On leave from the Department of Theoretical Physics, State University of Moldova, Kishinev, Republic of Moldova

†Corresponding author; balandin@ee.ucr.edu

- ¹A. Marti *et al.*, *Thin Solid Films* **511-512**, 638 (2006); S. Suraprapich *et al.*, *Sol. Energy Mater. Sol. Cells* **90**, 2968 (2006).
- ²M. A. Green, *Photovoltaic Applications of Nanostructures in the Handbook of Semiconductor Nanostructures and Nanodevices* (American Scientific Publishers, Los Angeles, 2006), Vol. 4, pp. 219–239.
- ³J. Phillips, *J. Appl. Phys.* **91**, 4590 (2002).
- ⁴J. L. Liu, W. G. Wu, A. Balandin, G. L. Jin, and K. L. Wang, *Appl. Phys. Lett.* **74**, 185 (1999); J. L. Liu, W. G. Wu, A. Balandin, G. L. Jin, Y. H. Luo, S. G. Thomas, Y. Lu, and K. L. Wang, *ibid.* **75**, 1745 (1999).
- ⁵V. Y. Aleshkin, N. A. Bekin, N. G. Kalugin, Z. F. Krasilnik, A. V. Novikov, V. V. Postnikov, and H. Seyringer, *JETP Lett.* **67**, 48 (1998).
- ⁶T. C. Harman, P. J. Taylor, D. L. Spears, and M. P. Walsh, *J. Electron. Mater.* **29**, L1 (2000).
- ⁷A. A. Balandin and O. L. Lazarenkova, *Appl. Phys. Lett.* **82**, 415 (2003).
- ⁸Y. Bao, W. L. Liu, M. Shamsa, K. Alim, A. A. Balandin, and J. L. Liu, *J. Electrochem. Soc.* **152**, G432 (2005); A. Khitun, A. Balandin, J. L. Liu, and K. L. Wang, *J. Appl. Phys.* **88**, 696 (2000).
- ⁹S. Bandyopadhyay, *Phys. Rev. B* **61**, 13813 (2000); S. Bandyopadhyay, A. Balandin, V. Roychowdhury, and F. Vatan, *Superlattices Microstruct.* **23**, 445 (1998); S. Bandyopadhyay and M. Cahay, *ibid.* **32**, 171 (2002).
- ¹⁰A. Balandin, G. Jin, and K. L. Wang, *J. Electron. Mater.* **20**, 549 (2000).
- ¹¹V. M. Fomin, V. N. Gladilin, J. T. Devreese, E. P. Pokatilov, S. N. Balaban, and S. N. Klimin, *Phys. Rev. B* **57**, 2415 (1998).
- ¹²V. A. Fonoberov and A. A. Balandin, *J. Nanoelectron. Optoelectron.* **1**, 19 (2006).
- ¹³O. L. Lazarenkova and A. Balandin, *J. Appl. Phys.* **89**, 5509 (2001).
- ¹⁴O. L. Lazarenkova and A. A. Balandin, *Phys. Rev. B* **66**, 245319 (2002).
- ¹⁵M. V. Artemyev, A. I. Bibik, L. I. Gurinovich, S. V. Gaponenko, and U. Woggon, *Phys. Rev. B* **60**, 1504 (1999).
- ¹⁶H. Z. Song, K. Akahane, S. Lan, H. Z. Xu, Y. Okada, and M. Kawabe, *Phys. Rev. B* **64**, 085303 (2001).
- ¹⁷J. S. Wang, S. H. Yu, Y. R. Lin, H. H. Lin, C. S. Yang, T. T. Chen, Y. F. Chen, G. W. Shu, J. L. Shen, R. S. Hsiao, J. F. Chen, and J. Y. Chi, *Nanotechnology* **18**, 015401 (2007).
- ¹⁸Y. Wang, H. S. Djie, and B. S. Ooi, *Appl. Phys. Lett.* **89**, 151104 (2006).
- ¹⁹A. J. Chiquito, M. G. de Souza, I. Camps, and Y. G. Gobato, *Semicond. Sci. Technol.* **21**, 912 (2006).
- ²⁰W. Zhang, K. Uesugi, and I. Suemune, *J. Appl. Phys.* **99**, 103103 (2006).
- ²¹F. F. Schrey, L. Rebohle, T. Muller, G. Strasser, K. Unterrainer, D. P. Nguyen, N. Regnault, R. Ferreira, and G. Bastard, *Phys. Rev. B* **72**, 155310 (2005).
- ²²T. v. Lippen, R. Notzel, G. J. Hamhuis, and J. H. Wolter, *J. Cryst. Growth* **278**, 88 (2005).
- ²³T. v. Lippen, R. Notzel, G. J. Hamhuis, and J. H. Wolter, *Appl. Phys. Lett.* **85**, 118 (2004).
- ²⁴Z. H. Zhang and K. Y. Cheng, *Appl. Phys. Lett.* **83**, 3183 (2003).
- ²⁵B. Kochman and A. D. Stiff-Roberts, *IEEE J. Quantum Electron.* **39**, 459 (2003).
- ²⁶G. Springholz, M. Pinczolics, P. Mayer, V. Holy, G. Bauer, H. H. Kang, and L. Salamanca-Riba, *Phys. Rev. Lett.* **84**, 4669 (2000).
- ²⁷O. Stier, M. Grundmann, and D. Bimberg, *Phys. Rev. B* **59**, 5688 (1999).
- ²⁸E. P. Pokatilov, V. A. Fonoberov, V. M. Fomin, and J. T. Devreese, *Phys. Rev. B* **64**, 245328 (2001).
- ²⁹B. A. Foreman, *Phys. Rev. B* **56**, R12748 (1997).
- ³⁰I. Vurgaftman, J. R. Meyer, and L. R. Ram-Mohan, *J. Appl. Phys.* **89**, 5815 (2001).
- ³¹Chu-Wei Jiang and Martin A. Green, *J. Appl. Phys.* **99**, 114902 (2006).
- ³²V. A. Fonoberov, E. P. Pokatilov, V. M. Fomin, and J. T. Devreese, *Phys. Rev. Lett.* **92**, 127402 (2004).
- ³³V. I. Klimov, A. A. Mikhailovskij, D. W. Mc. Branch, A. C. Leatherdele, and M. G. Bawendi, *Science* **287**, 1011 (2000).
- ³⁴V. I. Klimov *et al.*, *Science* **290**, 314 (2000).